International Journal of Machine Tools & Manufacture 206 (2025) 104247

Contents lists available at ScienceDirect

International Journal of Machine Tools and Manufacture

journal homepage: www.elsevier.com/locate/ijmactool

Research Article

Atomic-level insight into sequential evolution of nanocomposite carbon structures in femtosecond laser processing of diamond

Huili Han, Hao Liu, Jiaxu Huang, Pei Qiu, Jun Li, Bi Zhang *, Shaolin Xu **

Department of Mechanical and Energy Engineering, Southern University of Science and Technology, 1088 Xueyuan Avenue, Shenzhen, 518055, China

ARTICLE INFO

Keywords:
Femtosecond laser processing
Diamond
Nanocomposite carbon structure
Phase transition
Surface nanostructure

ABSTRACT

Diamond is an exceptional wide-bandgap semiconductor for electronics and quantum technologies. While femtosecond laser processing enables micro/nano fabrication of diamond, the dynamic atomic-level structural evolution during this process remains poorly understood, despite its critical impact on advanced applications. In this work, we investigate the multi-stage structural evolution of diamond under femtosecond laser irradiation, uncovering new scientific findings under laser-induced extreme conditions. The continuous input of pulse energy facilitates the rearrangement of local carbon atoms in the modified layer and partial phase transition layer, transitioning them from thermodynamically unstable to stable states. We introduce a sequential evolution pathway of nanocomposite carbon structures, and reinterpret the phenomenon previously broadly defined as "graphitization". Specifically, the evolution of diaphite, diamond-OLC (onion-like carbon), and the transition from amorphous carbon to planar-oriented graphite are reported under femtosecond laser surface processing. These phase transitions are initiated by the rapid lattice heating, with their distribution influenced by near-field enhancement effects arisen from surface nanostructures. This work provides atomic-scale insights into diamond's response in femtosecond laser processing, offering a theoretical foundation for ultra-precision micro/nano fabrication of diamond and the development of functional carbon materials.

1. Introduction

Defects at the atomic level significantly impact the properties of semiconductor materials, making their study essential for developing cutting-edge atomic-level manufacturing techniques. For instance, atomic-scale steps on a semiconductor substrate surface can affect the quality of wafer-scale single-crystal thin films during epitaxial growth [1], while crystal defects forming color centers impart unique optical and electrical properties, enabling applications in quantum technology [2]. Diamond is an ideal material choice for high-performance chips and quantum devices, earning the reputation of "ultimate semiconductor" due to its ultrawide bandgap, exceptional thermal conductivity, and high carrier mobility [3]. Femtosecond laser processing offers unparalleled advantages for micro/nano fabrication of such traditionally difficult-to-machine diamond [4,5]. However, instantaneous energy deposition from femtosecond laser irradiation on materials creates localized extreme high-temperature and high-pressure environments, typically inducing irreversible changes in atomic structures (Fig. 1a). Although various experimental and simulation studies have explored surface ablation morphologies and subsurface defects, detailed understanding of dynamic atomic-level structural changes induced by femtosecond laser in wide-bandgap semiconductors, particularly single-crystal diamond, remains limited.

These structural changes depend heavily on nonlinear absorption processes, such as multiphoton absorption and impact ionization [6], which rapidly elevate electron temperatures to approximately 10^4 K [7]. Subsequent energy transfer to lattice triggers melting, solidification, and solid-state transitions, which generally breaks the original lattice. Therefore, surface structures formed by laser irradiation, such as craters, laser-induced periodic surface structure (LIPSS), and pillar-like structures, typically accompany subsurface defects [8,9]. A key characteristic of femtosecond laser processing of diamond is the nanoscale phase transition, which has been broadly defined as "graphitization" in previous studies based on Raman spectroscopy. The immense energy provided by femtosecond lasers can cause the tetrahedrally connected sp^3-bonded diamond network to break and recombine, forming sp^3-bonded amorphous carbon [10], sp^2 clusters [11], and sp^1 metastable phase [12]. Due to the diversity of carbon allotropes, even

* Corresponding author.
** Corresponding author.
E-mail addresses: zhangb@sustech.edu.cn (B. Zhang), xusl@sustech.edu.cn (S. Xu).

https://doi.org/10.1016/j.ijmachtools.2025.104247
Received 24 September 2024; Received in revised form 3 January 2025; Accepted 15 January 2025
Available online 18 January 2025

identical carbon bonding can result in different phases with distinctive optical, electronic, and mechanical properties [13,14]. Transmission electron microscopy (TEM) is essential for identifying these phases. For instance, Hsu et al. [15] observed a tens-of-nanometer modified layer capping the irradiated diamond site, while Rehman et al. [16] identified a layer of amorphous carbon enclosing nanographite structures. Salter et al. [17] reported mixed sp^3–sp^2 bonded complexes termed "diaphite" in modified internal tracks. These studies highlight the complexity of phase transitions in diamond. Nevertheless, existing research has predominantly focused on isolated carbon phases under specific experimental parameters, leaving gaps in understanding the multi-stage progression of phase transitions during femtosecond laser surface processing.

Femtosecond laser processing with varying equivalent pulse numbers is typically required to meet different manufacturing demands. For example, single or few pulses are used for applications requiring extremely high precision, such as surface nanopatterning [18], while moderate pulse numbers introduce LIPSS for surface functionalization [15]. High pulse number are enable deep material removal for fabricating microholes/grooves and complex 3D structures [19]. The ultrafast dynamic process is repeated when laser pulses continuously act on the diamond surface [20]. The irreversible structural changes induced by early pulses fundamentally alter the material's current state, influence subsequent laser-materials interactions, and potentially leading to sequential evolution in surface and subsurface structures. As shown in Fig. 1b, the dynamic evolution of diamond structures under multi-pulse processing remains poorly understood but holds significant theoretical value for advancing the application of femtosecond lasers across different manufacturing demands.

In this work, we focus on the dynamic structural evolution in diamond during femtosecond laser multi-pulse processing, spanning from nanoscale material removal to LIPSS formation and deep materials removal. Using high-resolution transmission electron microscopy (HRTEM) and advanced analytical techniques, we uncover a novel sequential evolution mechanism of nanocomposite carbon structures. As laser pulse accumulation, the modified layer transitions from amorphous to amorphous-nanographite to planar-oriented graphite (POG), while the partial phase transition layer evolves from diaphite to diamond-OLC (onion-like carbon) to diamond-POG. These nanocarbon structures' distribution, unique phase transition pathways, and formation mechanisms are discussed by comprehensively considering ultrafast dynamics, electric field distribution, carbon material properties, and the ablation process. This work lays a theoretical foundation for ultra-precision micro/nano fabrication of diamond and opens new possibilities for developing novel functional carbon materials.

2. Material and methods

2.1. Materials and laser processing

The single-crystal diamonds used in this work were synthesized via high-pressure and high-temperature techniques by Element Six, with dimensions of 3 × 3 × 1 mm. The sample surfaces have a {100} crystal orientation and were polished to a final roughness of around 1 nm by Shenzhen Xinjinquan Precision Technology Co., Ltd. Before and after laser irradiation, all samples were ultrasonically cleaned in alcohol for 10 min to remove surface impurities.

The femtosecond laser processing equipment is shown in Fig. 2. A laser (SpOne-8-F2P-SHG, Spectra Physics) emits linearly polarized laser pulses with a central wavelength of 520 nm, a pulse duration of 300 fs, and a maximum output power of 5 W. A motorized half-wave plate and a Glan-laser polarizer are combined to precisely control the pulse energy. A beam expansion and collimation system, composed of a concave lens and a convex lens, is used to enlarge the laser beam diameter and optimize focusing performance. The laser beam is focused on a sample surface through a 20 × microscope objective (NA = 0.45, Nikon). An ultra-precision *XYZ* displacement platform (XMS100-S, Newport) with a minimum incremental motion of 10 nm in the *X* and *Y* directions ensures precise sample positioning and consistent laser pulse overlap. The waist radius ω_0(at $1/e^2$) of the focused Gaussian beam was measured to be 1.47 μm by analyzing the ablation crater sizes created at different pulse energies using the D-squared method (detailed description in Appendix 1). The damage threshold pulse energy E_{th} was calculated to be 139.7 nJ, with the corresponding ablation threshold $F_{th} = 2E_{th}/\pi\omega_0^2 = 4.12$ J cm^{-2}. The obtained ablation threshold is consistent with previously reported values for femtosecond laser ablation of diamond surfaces, ranging from 4 to 6.2 J cm^{-2} [21,22]. The reported differences are primarily attributed to variations in laser parameters, such as pulse duration and wavelength, which influence energy absorption and ablation dynamics. The single-pulse energy used in the multi-pulse processing

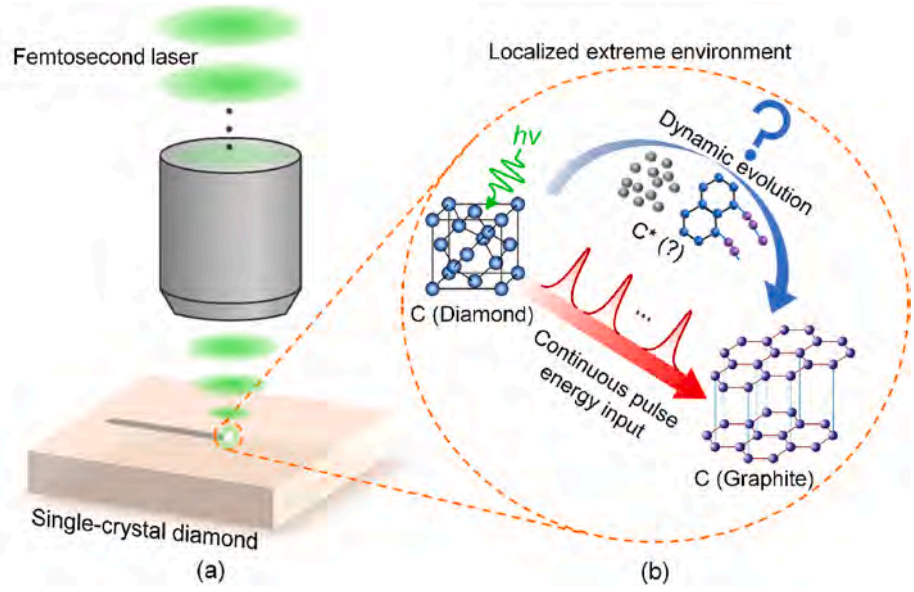

Fig. 1. Schematic representation of the key research issues in diamond phase transitions under femtosecond laser processing. (a) Femtosecond laser pulses create localized extreme conditions on single-crystal diamond. (b) The transition from sp^3-bonded diamond to sp^2-bonded graphite, with dynamic evolution stages induced by the multi-pulse energy input remaining unclear.

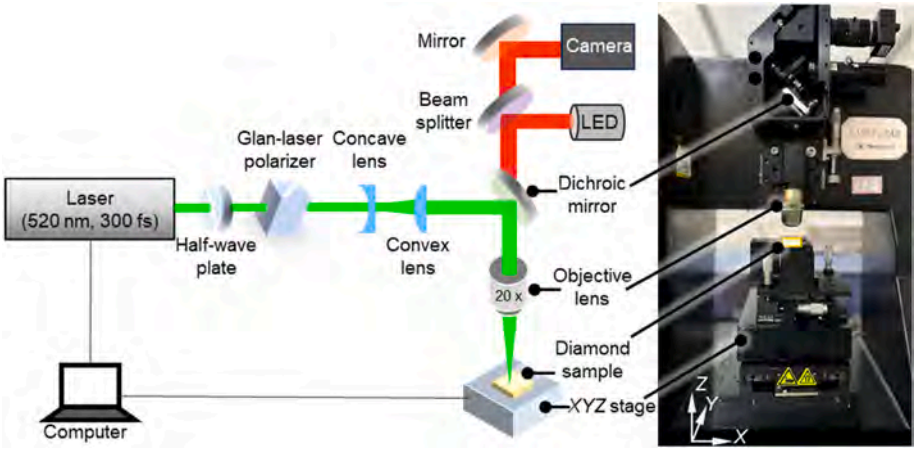

Fig. 2. Schematic diagram and photograph of the laser processing equipment.

experiment was fixed at 150 nJ, corresponding to a peak fluence of 4.42 J cm^{-2}, slightly above the ablation threshold, was chosen to ensure stable material processing while allowing for a gradual and observable phase evolution under multi-pulse irradiation.

2.2. Characterization and simulations

The morphologies of the irradiated samples were characterized via a scanning electron microscope (SEM) (FEI, Apreo 2S) and an atomic force microscope (AFM) (Bruker, Dimension edge). Raman spectra were collected under ambient conditions using a confocal micro-Raman system (HORIBA, LabRAM HR Evolution) equipped with a 532 nm laser excitation source and a spectral resolution of 2 cm^{-1}. A 100 × objective produced a focused laser spot of ~2 μm in diameter, delivering ~0.2 mW of laser power to the sample to minimize possible local heating effects during measurement. The focused ion beam (FIB) (FEI, Helios 600i) milling method was used to extract transmission electron microscopy (TEM) lamellas at fixed points (Fig. A2). To minimize the Ga-ion-induced damage and preserve the subsurface structure of the processed diamond, a ~9 nm Pt layer was sputtered onto the sample surface using a sputter coater (Quorum, Q150TES) prior to FIB coating and milling. The atomic structures and element distribution of subsurfaces were analyzed via TEM (FEI, Talos F200X G2).

The electric field intensity distributions for surface nanostructures were simulated using Finite-Difference Time-Domain (FDTD) commercial software (Lumerical 2020 R2, ANSYS). The simulation region, which includes an air layer and a diamond sample with surface nanostructures of various shapes, was enclosed by two perfectly matched layers (PML). Periodic boundary conditions were applied along the X and Y axes, with a plane wave source introduced in the simulation.

The ultrafast dynamic process of femtosecond laser interaction with single crystal diamond was numerically simulated using MATLAB R2022b academic software. We employed an improved Two-Temperature Model (TTM) optimized by previous researchers [23], which accounts for variations in carrier density and is suitable for simulating the interaction between femtosecond laser pulses and single-crystal diamonds, enabling the predicting of phase transitions:

$$C_e\frac{\partial T_e}{\partial t}=\frac{\partial}{\partial x}\left(k_e\frac{\partial T_e}{\partial x}\right)-g(T_e-T_l)+Q \tag{1}$$

$$C_l\frac{\partial T_l}{\partial t}=\frac{\partial}{\partial x}\left(k_l\frac{\partial T_l}{\partial x}\right)+g(T_e-T_l) \tag{2}$$

where T_e is the electron temperature, T_l is the lattice temperature, C_e is the electron heat capacity, C_l is the lattice heat capacity, k_e is the electron heat conductivity, k_l is the lattice heat conductivity, g is the coupling coefficient between the electron and lattice, and Q is the heat source term. As a wide-bandgap material, diamond initially lacks sufficient free carriers in the conduction band. Upon instantaneous irradiation with femtosecond laser pulses, a large number of valence electrons, initially bound within covalent bonds, are excited and transition to the conduction band, resulting in a dramatic increase in surface carrier density. Considering mechanisms such as single and two-photon absorption, impact ionization, carrier diffusion, and Auger recombination, the evolution of the carrier density n_e over time is governed by the following Equation [24]:

$$\frac{\partial n_e}{\partial t}=\frac{\partial}{\partial x}\left(D_0\frac{\partial n_e}{\partial x}\right)-\gamma n_e^3+\eta n_e+\frac{\alpha I}{h\nu}+\frac{\beta I^2}{h\nu} \tag{3}$$

where D_0 is the ambipolar diffusivity, γ is the Auger recombination coefficient, η is the impact ionization coefficient, α is the single-photon absorption coefficient, β is the two-photon absorption coefficient, I is the laser intensity, and $h\nu$ is the photon energy. The specific calculation details are shown in Appendix 3.

3. Results

3.1. Surface micro/nano morphology

A series of multi-pulse femtosecond laser processing experiments were carried out on the diamond surface, and the resulting surface micro/nano morphologies are shown in Fig. 3. The equivalent pulse number for line scanning can be calculated by $N = 2\omega_0 f/v$, where f is the laser repetition rate, and v represents the laser scanning speed. As pulse accumulation, the surface processed by laser line scanning transitions from isolated shallow pits to LIPSS and then to microgrooves of increasing depth (Fig. 3a–d), exhibiting a consistent pattern with the changes observed in point processing (Fig. 3e–h). Line scanning can be considered as an extension of point processing in space, as the energy distribution of laser pulses within the material is essentially similar. Therefore, the interaction mechanisms between the laser and materials are often studied using point processing experiments. In the following sections, we further analyze the results of point processing to reveal the commonly observed structural evolution and its underlying causes. In the point processing results, after a single pulse irradiation, tiny nanopits are observed within the pit morphology (Fig. 3e). As the pulse number increases, surface ripples gradually emerge, leading to the formation of distinct LIPSS perpendicular to the polarization direction after approximately 10 pulses (Fig. 3f). The detailed morphology evolution is shown in Fig. A4. The widely accepted explanation for the formation of LIPSS is the interference between the incident laser and surface plasmon polaritons (SPPs) [25]. In the initial stage of laser pulse irradiation, the

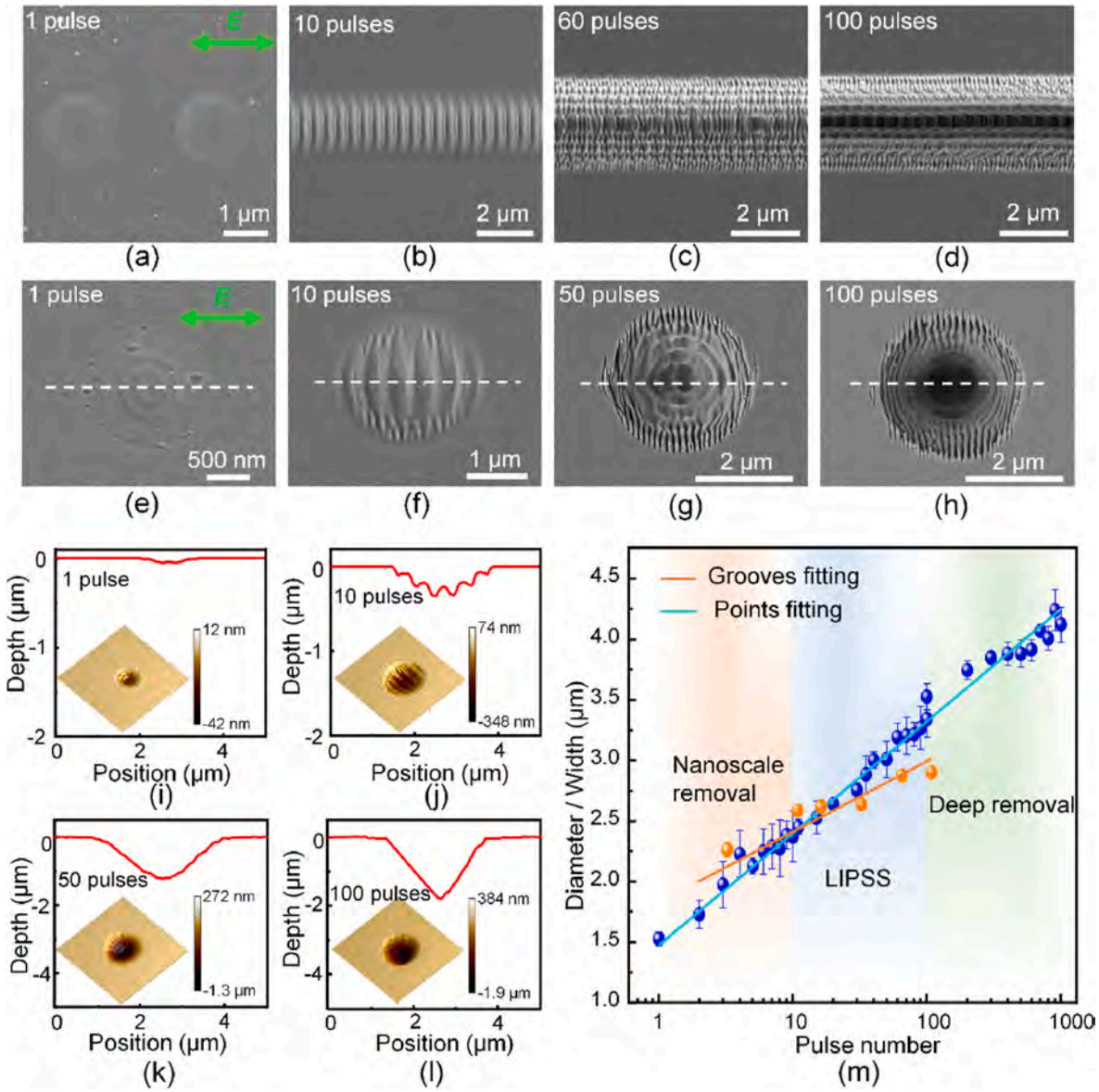

Fig. 3. Typical surface ablation morphologies by femtosecond laser irradiation. (a–d) SEM images of surface morphologies with 1, 10, 60, and 100 pulses in line scanning processing, respectively. (e–h) SEM images of surface morphologies with 1, 10, 50, and 100 pulses in point processing, respectively. The white dotted lines indicate the direction for subsequent FIB extraction of TEM samples. (i–l) AFM characterization of ablation structure and cross-sectional profile curves with different pulse numbers. (m) Dependence of the diamond ablation diameter/width on the pulse number.

mismatch in momentum—vertical for the incident light and horizontal for SPPs—prevents the direct generation of SPPs. However, as pulse accumulation reaches around 10 pulses, the uneven surface created by prior ablation provides the necessary scattering conditions, generating horizontal momentum that fulfills the conditions required for LIPSS formation. The morphology of LIPSS evolves continuously with increasing pulse numbers (Fig. 3g), with the central region deepening gradually into a microhole at around 100 pulses (Fig. 3h). In SEM images of the material surface within the 1-1,000 pulse range, there are some nanometer-sized particles (Fig. A4) generated from the redeposition of the ejected bulk materials [26].

The AFM characterization results in Fig. 3i show that the material is removed to a depth of approximately 40 nm from the surface after a single pulse. Subsequently, the material removal depth increases rapidly; at 10 pulses, the material removal depth reaches around 350 nm when LIPSS forms on the surface (Fig. 3j). At 50 pulses, the depth reaches approximately 1.3 μm for the formation of cavities (Fig. 3k), and at 100 pulses, it deepens to 1.9 μm (Fig. 3l). According to the surface morphology and characteristic depth observed in both line scanning and point processing, the evolution of diamond surface structures with pulse accumulation can be divided into three regions, as shown in Fig. 3m. When the pulse number is less than 10, it can be classified into the nanoscale removal stage; at 10–100 pulses, it is the LIPSS stage; and after reaching 100 pulses, it enters the deep removal stage. It has to be mentioned that the LIPSS morphology continuously exists in strong ablation condition. The point processing morphology with different laser pulse intervals also exhibits a consistent change trend (see Appendix 6). Statistical analysis in Fig. 3m reveals that regardless of the surface morphology induced by irradiation, the diameter/width of surface structures increases with the pulse number and exhibits an approximately linear relationship with the natural logarithm of the pulse number.

To analyze the phase transition characteristics associated with different surface structures, we first employed Raman spectroscopy to examine diamonds irradiated with varying pulse numbers. As depicted in Fig. 4a, all samples exhibit a distinct intrinsic sp^3 tetrahedral diamond

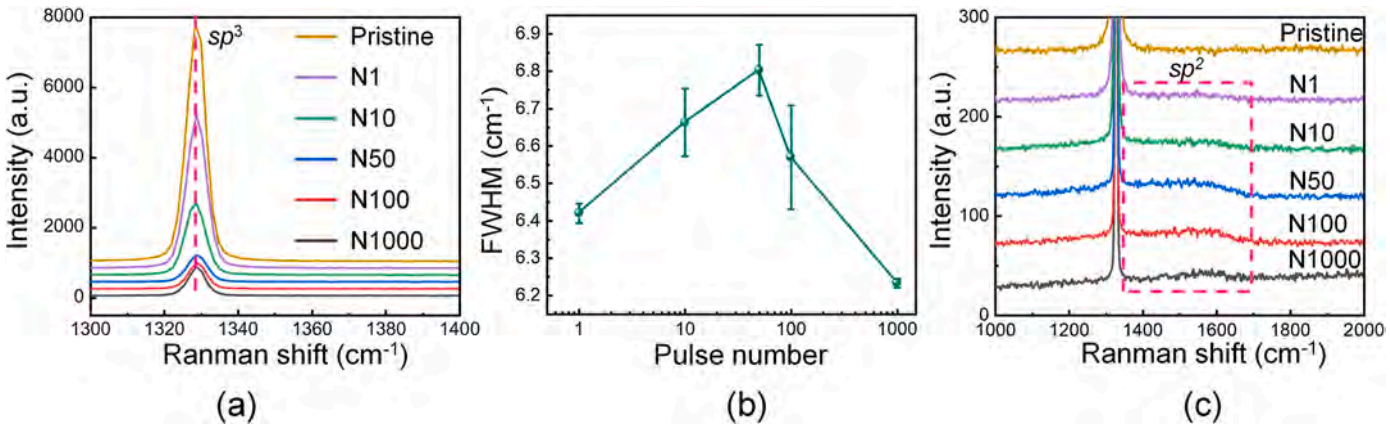

Fig. 4. Raman spectra at the center of the surface structures. (a) Raman peak characteristics of sp^3-bonded carbon. (b) FWHM of the diamond peak obtained through Gaussian fitting. (c) Raman peak characteristics of sp^2-bonded carbon.

T_{2g} stretching mode at ~1,329 cm^{-1}. In the early stages of pulse accumulation, the intensity of the diamond peak decreases, accompanied by an increase in the full width at half maximum (FWHM) (Fig. 4b). Simultaneously, the background signal shows a broad band emerging in the range of 1,350–1,700 cm^{-1} (Fig. 4c). This broadband feature formed by merging the D and G vibrational modes (~1,350 cm^{-1} and ~1,582 cm^{-1}, respectively), corresponding to the defective sp^2 carbon structures [12,27] These spectral features suggest that the early stages of laser pulse accumulation disrupt the crystalline integrity of the diamond, introducing more lattice defects and triggering localized near-surface amorphization and the formation of graphitic-like phases.

However, when the pulse number reaches 100, the FWHM of the diamond peak begins to decrease, and the intensity of the broadband associated with sp^2 carbon structures does not significantly increase (Fig. 4c). This indicates that at higher pulse numbers, the graphitization on the surface reaches a stable state, and the diamond structure contains fewer defects rather than experiencing further damage accumulation [28]. This trend may result from the removal of defective material via ablation or the reconstruction of surface carbon, which reduces the structural disorder.

Throughout the 1-1,000 pulses range, the intensity of the broadband associated with sp^2 carbon structures is much weaker compared to the diamond peak, indicating that laser pulses only affect an extremely thin surface layer, with only a small portion of sp^3 bonded carbon converted into sp^2 bonded carbon. To further clarify the mixed sp^2 and sp^3 bonded carbon phases, as well as the subsurface defect distribution and evolution of the thin irradiation-affected layer, an additional TEM analysis is essential.

3.2. Atomic-level subsurface structural characteristics

3.2.1. Graphite nucleation within diamond lattice in nanoscale removal stage

We selected samples from three distinct stages of surface structure evolution—nanoscale removal, LIPSS, and deep removal—for atomic-scale subsurface analysis, offering new insights into the phenomena accompanying pulse accumulation. After irradiation, three distinct layers were identified in the subsurface of the diamond: the modified layer, partial phase transition layer, and unaffected layer. Fig. 5a demonstrates the entire view of the subsurface features of the pit structure, and the inset shows a typical selected area electron diffraction (SAED) pattern viewed along the [001] zone axis of the diamond. Fig. 5b and c shows the magnified features of this pit morphology through the cross-section morphology and elemental distribution information, respectively. The topmost layer is a deposited Pt protective layer, followed by a modified layer with an average thickness of ~34 nm formed on the surface of the irradiated sample. Beneath the modified layer is a partial phase transition layer containing a few defects and an unaffected layer. The HRTEM observations revealed the atomic-resolution structures of irradiated diamonds and showed the diverse carbon structures during the femtosecond laser-induced phase transition. The modified layer consists of disordered arrangement of amorphous carbon (Fig. 5d). The inserted FFT image in Fig. 5d shows a diffuse ring pattern without distinct diffraction spots, indicating the absence of typical long-range order of crystalline structures. The material removal below the surface in the nanoscale removal stage may be due to the sublimation of amorphous diamond. Compared to crystalline diamond, the amorphous diamond on the surface lacks long-range order, making it less thermally stable and more prone to sublimation. The unaffected layer (Fig. 5e) displays a narrow lattice spacing of 0.13 nm, corresponding to the (220) plane of diamond.

Graphitization is generally believed to start from defects on the diamond surface. These defects which provide a lower energy barrier for the phase transition due to increased surface energy. It is worth noting that a small amount of sp^3 bonds is broken at this stage due to the graphite nucleation within diamond lattice rather than surface, which is the formation of graphite nanocrystals with a size of 2.9–5.5 nm in the partial phase transition layer shown in Fig. 5f (marked with white circles). The corresponding fast Fourier transform (FFT) image (inset in Fig. 5f) containing both diamond diffraction spots and diffraction rings from graphite planes, confirms this biphasic structure. Fig. 5g and h exhibit magnified features of the nanographite crystals and the interface characteristics with the diamond phase. Within the (220) crystal plane of diamond, layers with lattice spacing of 0.35 nm are formed, corresponding to the interlayer (002) plane of graphite. These nanosized (002) graphitic sheets are parallel to or at an angle to the diamond (220) plane; some are slightly curved. This composite carbon structure, known as “diaphite” [13], consists of graphitic/graphene-like sp^2 layers inserted into sp^3-bonded domains. It is a metastable phase that is difficult to synthesize, typically forming under extreme conditions such as extraterrestrial impacts or high-temperature and high-pressure environments. The combination of sp^3 diamond and sp^2 graphite nanodomains gives this phase unique mechanical, thermal, and optoelectronic properties [13,14]. While diaphite has previously been observed in femtosecond laser-written tracks within the interior of diamond [17], this is the first instance of its identification under surface processing conditions. This discovery offers new perspectives for re-interpreting and analyzing the initiation of graphitization during femtosecond laser irradiation.

3.2.2. Onion-like carbon formation beneath LIPSS

The cross-sectional features of the LIPSS are depicted in Fig. 6a. It can be observed that some defect features are distributed around the corners of LIPSS. The HRTEM image of LIPSS waist below the modified

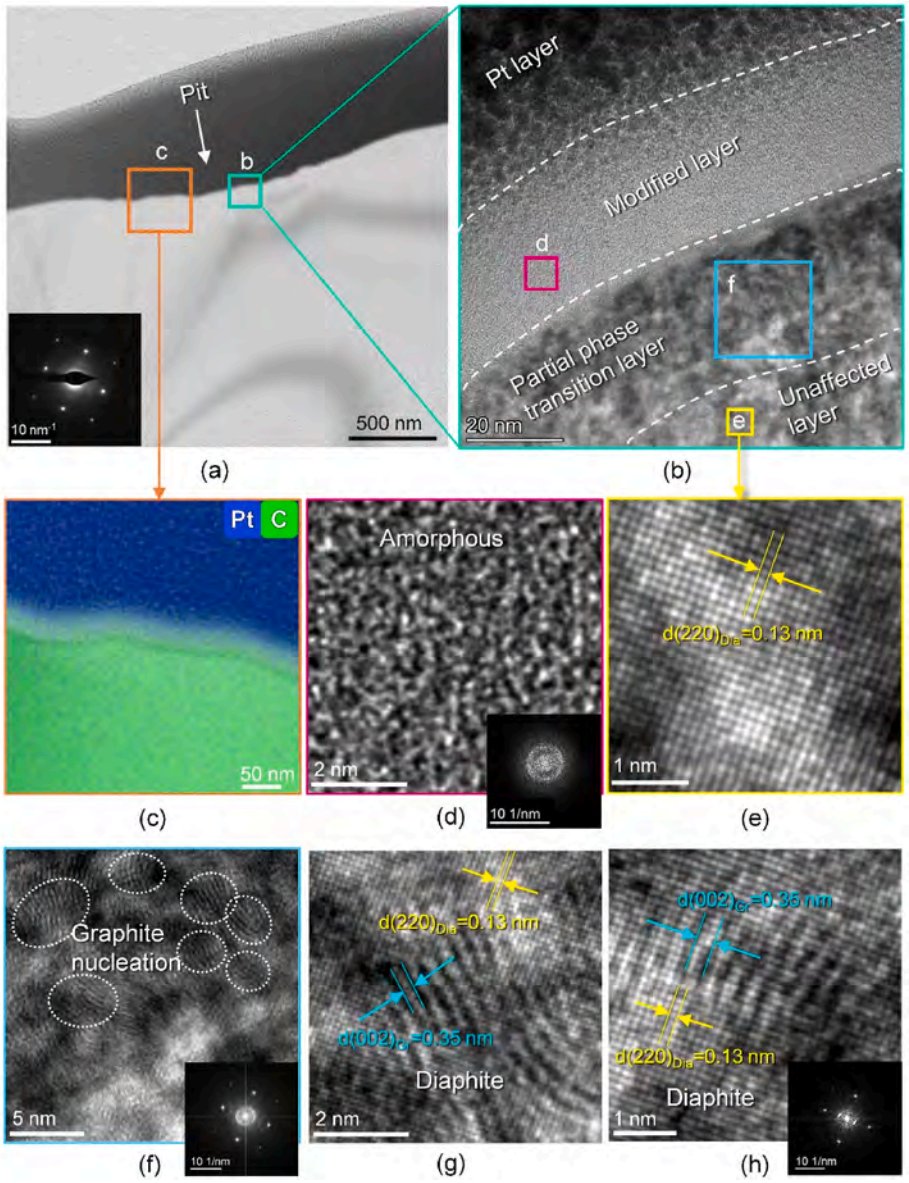

Fig. 5. Subsurface of pit formed after 1 pulse irradiation. (a) Overall subsurface landscape in bright-field mode; the inset shows the SAED pattern viewed along the [001] zone axis of diamond. (b) HRTEM image of the green area in (a). (c) Elements distribution in the orange area in (a), showing the boundary between the diamond and protective layer. (d) High magnification of modified layer characteristics in (b); the insert shows the corresponding FFT image, which indicates no crystalline structure. (e) High magnification of the unaffected layer in the yellow area in (b). (f) Enlarged image of the blue area in partial phase transition layer; the insert is the corresponding FFT image; the dashed circles show the graphite nucleation feature in diamond lattice. (g–h) High magnification of diaphite.

layer indicates that a diamond lattice structure is still maintained (as shown in the inset of Fig. 6b). The modified layer has an average thickness of 23 nm. Unlike the modified layer on the surface of pit morphology, which is composed of amorphous carbon, this layer contains some short incomplete graphitic crystalline planes embedded in amorphous (Fig. 6e). The plane spacing is approximately 0.34 nm, matching the (002) graphite plane. This composite structure is similar to the carbon structures observed by Rehman [16] in diamond after processing with a 40-fs laser at a fluence of 83 J cm^{-2} and 10 pulses. Compared to the initial stage of pulse accumulation, this transition reflects a tendency of disordered carbon atoms to reorganize into more stable, lower-energy ordered structures due to excess energy during processing. The transition of amorphous layer to graphite was also observed in annealed diamond after ion radiation damage, starting with the growth of sp^2 hybrid nanoclusters [29,30].

Additionally, another interesting finding is that at the corners of the LIPSS, local shading differences are caused by localized plastic deformation (Fig. 6a–c). A significant phase transition occurs in this region, evident in the HRTEM image (Fig. 6d), where numerous bent graphite shells within the diamond lattice are observed. The magnified features in the rectangular region illustrate the typical morphology of this carbon structure (Fig. 6f and g). Dozens of curved graphite shells make up the onion-like carbon (OLC) phase. This highly curved shell structure is confirmed by the annular diffraction spots of the (002) graphite plane in the corresponding FFT image (Fig. 6h). It is worth noting that this OLC-diamond composite structure is observed for the first time in diamond processed by femtosecond laser. This structure originates from the growth, bending, and closing of the nanographite layer in the initial stage, a process that reduces the number of dangling bonds and significantly reduces the surface energy [31,32]. OLC has already been applied in fields such as nanotribology, photocatalysis, and energy storage [33]. The formation of OLC during processing will slightly reduce the hardness of diamond while improving its toughness [34], significantly increasing optical absorption [35] and electrical

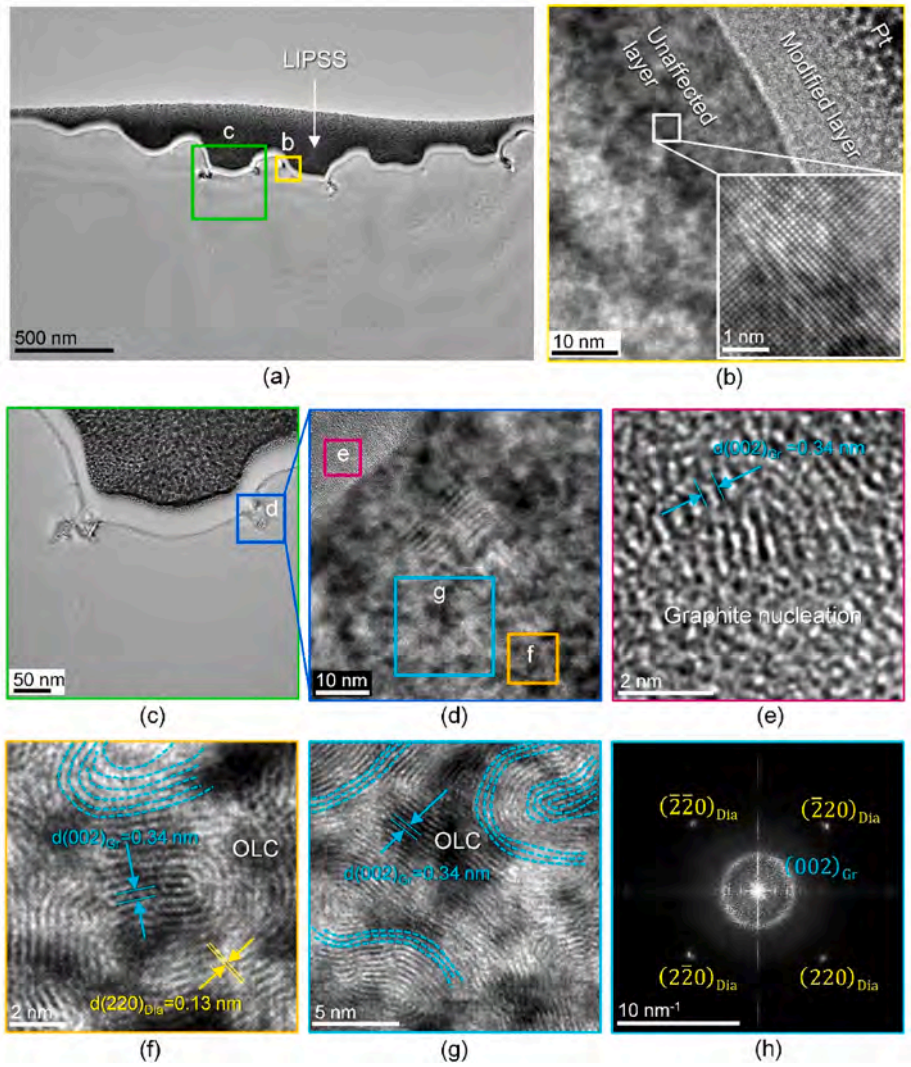

Fig. 6. Subsurface of LIPSS formed after 10 pulses irradiation. (a) Overall subsurface landscape in bright-field mode. (b) HRTEM image of the yellow area in (a); the inset is a high magnification of unaffected diamond lattice. (c) Enlarged view of the bottom of the LIPSS in (a). (d) HRTEM image of the green area in (c). (e) High magnification of the modified layer. (f–g) High magnification of OLC in the partial phase transition layer. (h) FFT image corresponding to (g), shows the highly curved nanographite basal planes.

conductivity [36].

Unlike the results from long-pulse diamond processing, the graphitization front does not exhibit a clear boundary. This unique phase transition distribution will be further analyzed in Section 3.3. Due to the different densities of graphite and diamond (2.265 and 3.515 g/cm^3, respectively), the phase transition inside the diamond causes volume expansion and local stress concentration. Under lower fluence, this manifests as plastic deformation at nanoscale, while under higher fluence irradiation, the local stress exceeds the tensile strength of diamond, leading to crack initiation, and the cracks tend to spread along {111} planes (see Fig. A1).

3.2.3. *Planar-oriented graphite formation in deep removal stage*

The cross-sectional features of the microhole morphology irradiated by 100 pulses are depicted in Fig. 7a, with a modified layer thickness of approximately 17 nm (Fig. 7b and c). An enlarged view of the modified region in Fig. 7d demonstrates enlarged graphite layers within the amorphous, forming ordered and parallel (002) layers. Compared to the modified layer in the LIPSS stage, which is characterized by an amorphous structure enveloping short, disordered graphite sheets, the accumulation of laser pulses further facilitates atomic rearrangement in more amorphous structures, transitioning the modified layer toward graphitization and forming an ordered POG structure. The corresponding inverse fast Fourier-transform (IFFT) image (Fig. 7e) reveals numerous lattice distortion defects within this POG structure. In the adjacent partial phase transition layer, the OLC present in LIPSS stage also evolves into POG after 100 pulses of irradiation (Fig. 7f and g). The graphite (002) planes merge to the diamond (220) planes. Due to the energy favorable of combining previously formed adjacent OLCs over independent OLCs generation, the curved graphite shells tend to expand and form parallel-oriented graphite bands [37]. This structure is thermodynamically more stable and is a common phase transition product driven by thermal effects during nanosecond laser processing [38] or high-temperature annealing (1800–2100 K). The corresponding FFT image showing two separated and symmetric diffraction arcs of graphite layers further confirms this oriented structural characteristic (Fig. 7h). The TEM results reveal the gradual transition of the modified layer and partial phase transition layer into POG with the accumulation of femtosecond pulses, showcasing the potential of ultrafast dynamic cycling to regulate carbon structures along non-equilibrium pathways. Moreover, the POG phase recovers to the pristine diamond lattice within a very narrow range of about 4 nm (Fig. 7g), demonstrating the femtosecond laser's minimal influence depth and the manufacturing capability of low subsurface damage under high pulse number

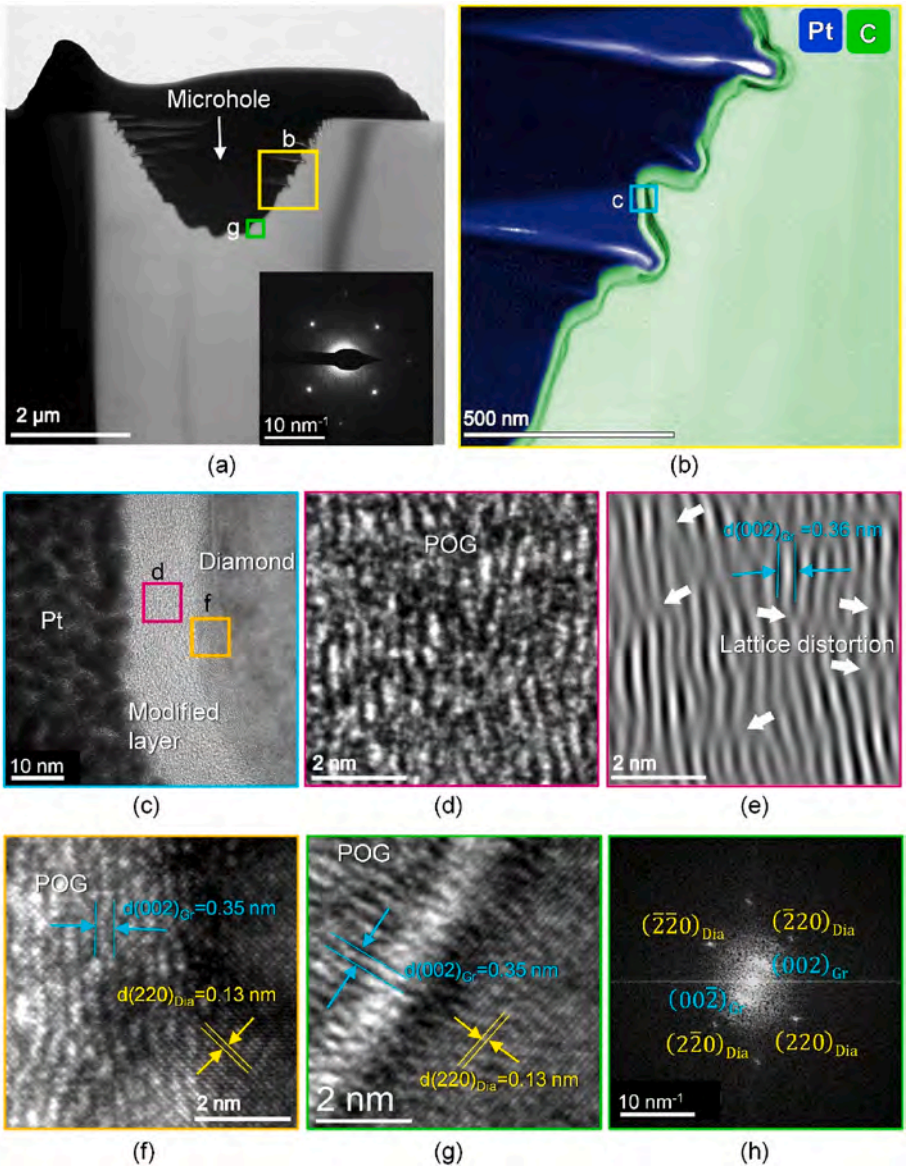

Fig. 7. Subsurface of mircohole after 100 pulses irradiation. (a) Overall subsurface landscape in bright-field mode; the inset shows the SAED pattern viewed along the [001] zone axis of diamond. (b) False color image highlighting element distribution and interface information. (c) HRTEM image of blue area in (b). (d) High magnification of the modified layer. (e) IFFT image corresponding to (d), shows numerous lattice distortion features of the POG phase in the modified layer. (f) High magnification of POG in the partial phase transition layer in (c). (g) High magnification of POG in partial phase transition layer at the bottom of cavity. (h) FFT image corresponding to (g), shows the (002) plane POG and (220) plane diamond composite carbon structure.

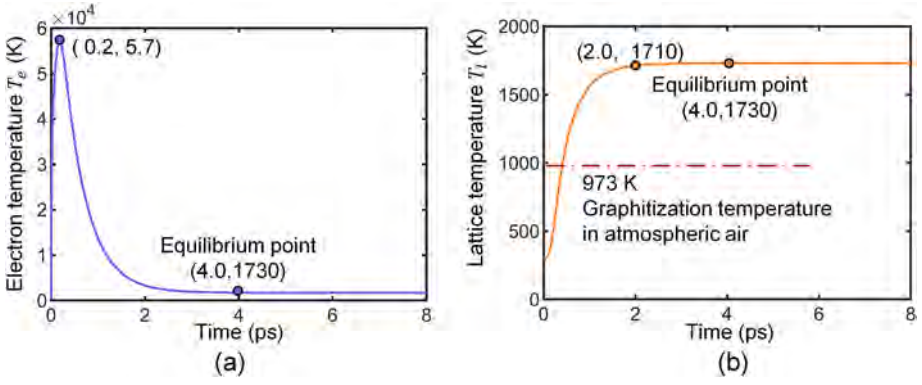

Fig. 8. Irradiation response of diamond under femtosecond laser. (a) Temporal evolution of electron temperature T_e. (b) Temporal evolution of lattice temperature T_l.

irradiation.

3.3. Physical origins of the defect evolution and distribution

Phase transition results from energy transfer during the interaction between femtosecond laser pulses and the material. The transfer of absorbed energy from electrons to the lattice provides the appropriate thermodynamic driving force for the phase transition to occur. Fig. 8 shows the TTM calculation results using the explicit finite difference method. The electron temperature (T_e) rapidly increases to approximately 5.7×10^4 K within the first 0.2 ps, followed by an exponential decay (Fig. 8a). The peak electron temperature indicates the intense energy absorption of the femtosecond laser pulse. The subsequent decay represents the cooling of the electron subsystem as energy is distributed to the lattice, leading to thermal equilibrium. This behavior aligns with the expected ultrafast dynamics in diamond, where high thermal conductivity facilitates rapid energy dissipation. The lattice temperature (T_l) shows a sharp rise, reaching around 1,710 K within 2 ps, and then plateaus to 1,730 K as it approaches thermal equilibrium with the electron subsystem at 4 ps (Fig. 8b). Due to the equilibrium temperature being higher than the graphitization temperature of diamond in atmospheric air, thermally activated graphitization is triggered. The nonlinear ionization process generates an electron density as high as 1.39×10^{21} cm^{-3} (Fig. A3), leading to the weakening and breaking of sp^3 carbon-carbon bonds, which destabilizes the local lattice and promotes its rearrangement into the thermodynamically more stable sp^2 configuration. This transition initiates the formation of graphite nucleation sites. Different pulse numbers resulted in varying rapid heating and cooling cycles, preserving diverse carbon structures with various degrees of graphitization at room temperature.

The changes in the thickness of the subsurface modified layer under multi-pulse processing, as shown in Fig. 9a, illustrate the trend from an unstable to a stable state. With an increase in the pulse number, the thickness of the modified layer tends to decrease, stabilizing after more than 100 pulses. The pulse interval used in the experiment was 1 ms, far exceeding the timescales of various electron and lattice processes in laser excitation (up to several microseconds), indicating that the crystal structures and surface micro/nanostructures formed by early pulses significantly affect subsequent laser pulses. Under laser irradiation of less than 100 pulses, the increased number of sp^2 bonded nanoclusters in amorphous and diamond with pulse superposition significantly enhances surface absorption. It limits the propagation of laser energy into the interior [39,40], leading to reduced modification depth. At the deep removal stage, the modified layer transitions into a thermodynamically stable POG layer, acting as a stable laser absorption layer. Consequently, the thickness of the modified layer no longer significantly decreases. Further laser pulses form deep and narrow nanostrips at the bottom of the microhole, with a depth of 2.3 μm and a width of only 60 nm, as shown in Fig. 9b and c. From the SAED pattern in Fig. 9c, this unique nanostructure still maintains a diamond lattice.

FDTD simulations complement the experimental studies and explain the unique phase distribution phenomenon associated with the processing. The results suggest that surface nanostructure features influence the distribution of electric field intensity, causing significant local enhancement. This near-field enhancement effect can lead to a sharp increase in temperature in localized regions, triggering phase transitions in specific areas. Shallow LIPSS formed around 10 pulses exhibit near-field enhancement effect at sharp tips (Fig. 10a–c). Compared to LIPSS with sharp bottom angles, the electric field intensity enhancement for smooth angles appears at the waist (Fig. 10d–f). This also aligns with observed defect distributions in Fig. 6, indicating a tendency for plastic deformation due to phase transition to concentrate at sharp corners of LIPSS structures. Surface nanostructures formed under high pulse number display enhanced electric field intensity at the middle and bottom of the nanostrips (Fig. 10g–i), which aid in intensifying sidewall and bottom ablation, further evolving into narrower and deeper nanostrips [41].

4. Discussion

Nanoscale phase transitions are a key feature of structural evolution under successive femtosecond laser pulse irradiation, significantly impacting diamond ablation and modification [4]. In this study, we focused on the dynamic, multi-stage structural evolution during femtosecond laser processing of diamond—a material with significant practical applications and diverse allotropes—and uncovered several novel scientific findings, including new phase transition pathways and mechanisms in the extreme environment induced by femtosecond lasers (Fig. 11). These findings also offer a re-interpretation of the initiation, evolution, and stabilization stages of laser-induced diamond phase

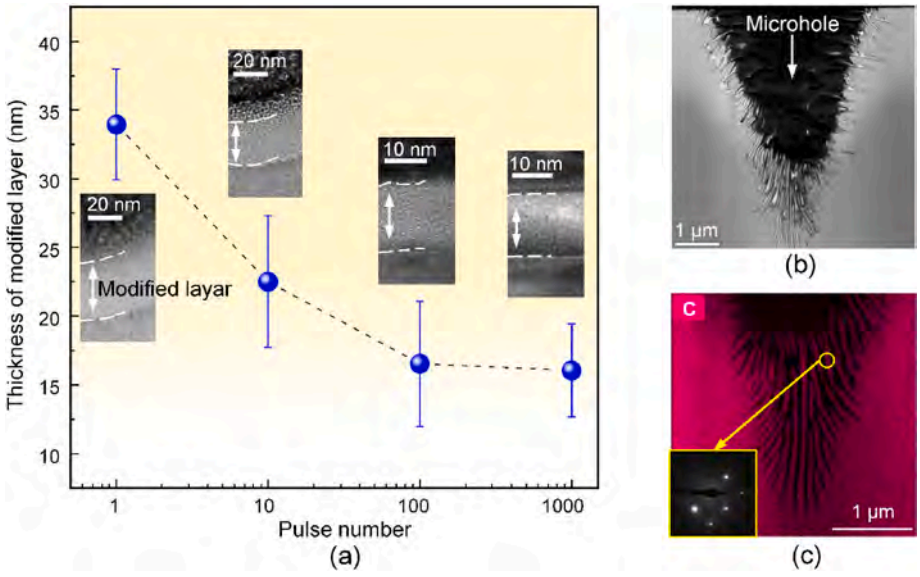

Fig. 9. Defect evolution and distribution. (a) Variation of the thickness of the modified layer with pulse number. (b) Overview of the subsurface of microhole formed by 1,000 pulses. (c) The nanostrips at the bottom of microhole, with the pink color indicating the elemental distribution of carbon; the inset shows the SAED pattern of the circled area, demonstrating that the nanostructure still maintains a diamond lattice.

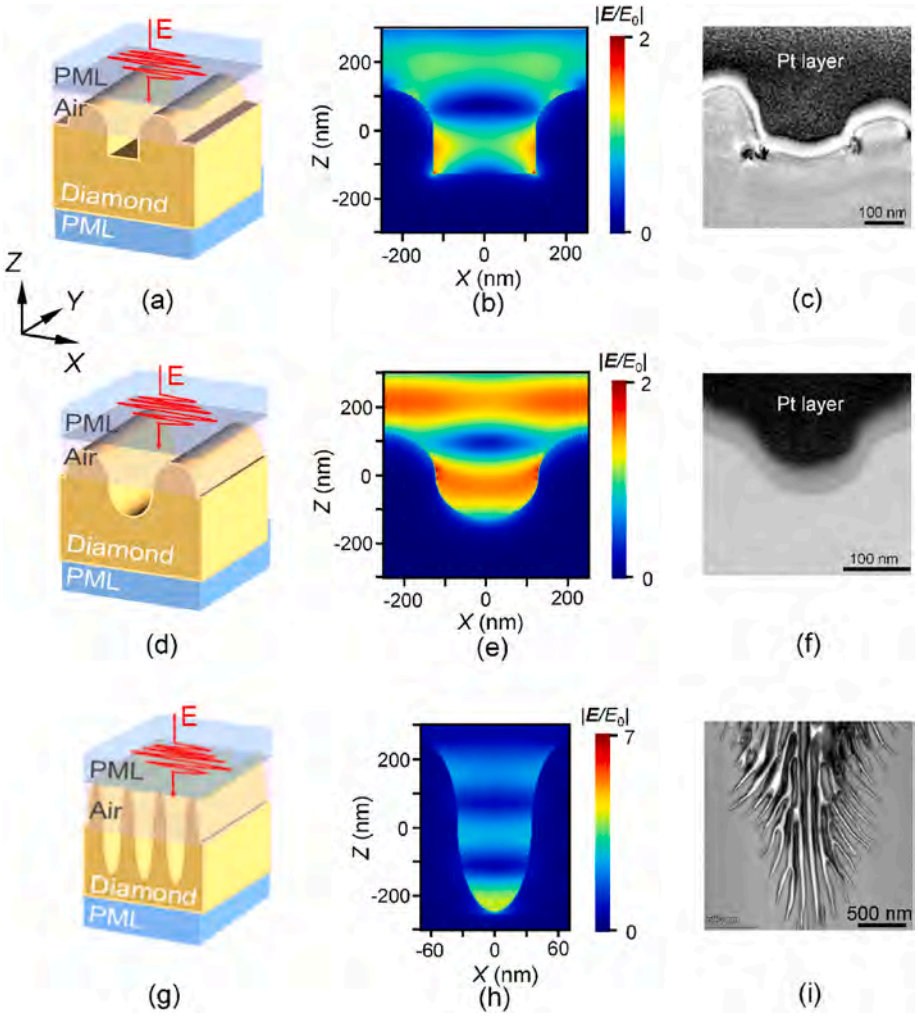

Fig. 10. FDTD simulations of the electric field distribution inside different surface nanostructures. (a) Schematic diagram of FDTD 3D simulation model for sharp corners LIPSS. The red arrow indicates both the polarization direction and the propagation direction of the wave. (b) The sectional electric field of LIPSS with sharp corners formed at low pulse number. (c) TEM of LIPSS with sharp corners. (d) Schematic diagram of FDTD 3D simulation model for smooth corners LIPSS. (e) The sectional electric field of LIPSS with smooth corners formed at low pulse number. (f) TEM of LIPSS with smooth corners. (g) Schematic diagram of FDTD 3D simulation model for deep nanostrips. (h) The sectional electric field of deep nanostrips formed at high pulse number. (i) TEM of deep nanostrips.

transition, previously broadly categorized as "graphitization".

In the initiation stage of pulse accumulation, extremely fast energy input disrupts the original crystal structure, causing amorphization and graphitization. The high inherent resistance of diamond to external impacts leads to rapid pressure decay with increasing material depth, creating a partial phase transition layer near the surface (Fig. 11a). This layer, a mixture of nanographite and diamond crystal, forms the diaphite phase. The accumulative graphitization model proposed by Kononenko et al. [42], which suggests that graphitization initiates from photostimulated formation of graphite microparticles, also supports our experimental results. Our findings show that graphitization nucleates unusually from the region below the modified layer, rather than starting from the surface defects (Fig. 11c). This can be attributed to the high transmittance of diamond in the visible light range, allowing partial energy to be deposited within the bulk rather than just at the surface, thereby creating favorable conditions for the formation of nanographite crystals. The surrounding diamond matrix also provides a high-pressure environment for the low-density nanographite sheets concentrated at a tiny scale [17]. This growth environment is similar to that of diaphite formation in meteoritic diamonds.

In the intermediate evolution stage of pulse accumulation, newly formed structures are continuously "quenched" by the thermal effect of the subsequent laser pulses [43]. When new pulse energy is introduced, the ionized carbon atoms at the graphite-diamond composite structure boundary are much more distorted than those within a perfect diamond lattice. These atoms are more prone to rearrangement or breaking, leading to the conversion of sp^3 bonds to sp^2 bonds and promoting the expansion of graphite planes, resulting in their self-evolution. The sp^2-bonded graphite layers formed within the laser-affected region and surface pits act as concave lenses, significantly reflecting and refocusing subsequent laser pulses [44]. These factors lead to enhanced absorption of the following pulse energy. Diamonds have very low fracture toughness, but the generation of sp^2-bonded carbon in matrix can promote the local plastic flow, enhance the stability of the structure because of the ductile bridging effect, and prevent the occurrence of cracks under a series of laser pulses [34]. Insulating diamond internally forms conductive nanochannels, transforming two-photon absorption into single-photon absorption, exciting more free electrons. Nanoablation transforms into graphitization ablation, and the depth of material removal spans from the nanoscale to the microscale.

In the final stabilization stage, the irradiated region of diamond becomes visibly black (Fig. A5), with the modified and partial transition layers composed of thermodynamically more stable planar-oriented graphite/graphene bands. As a semi-metal with absorption characteristics several orders of magnitude higher than diamond in the optical spectrum, POG confines laser energy to the surface, preventing deeper

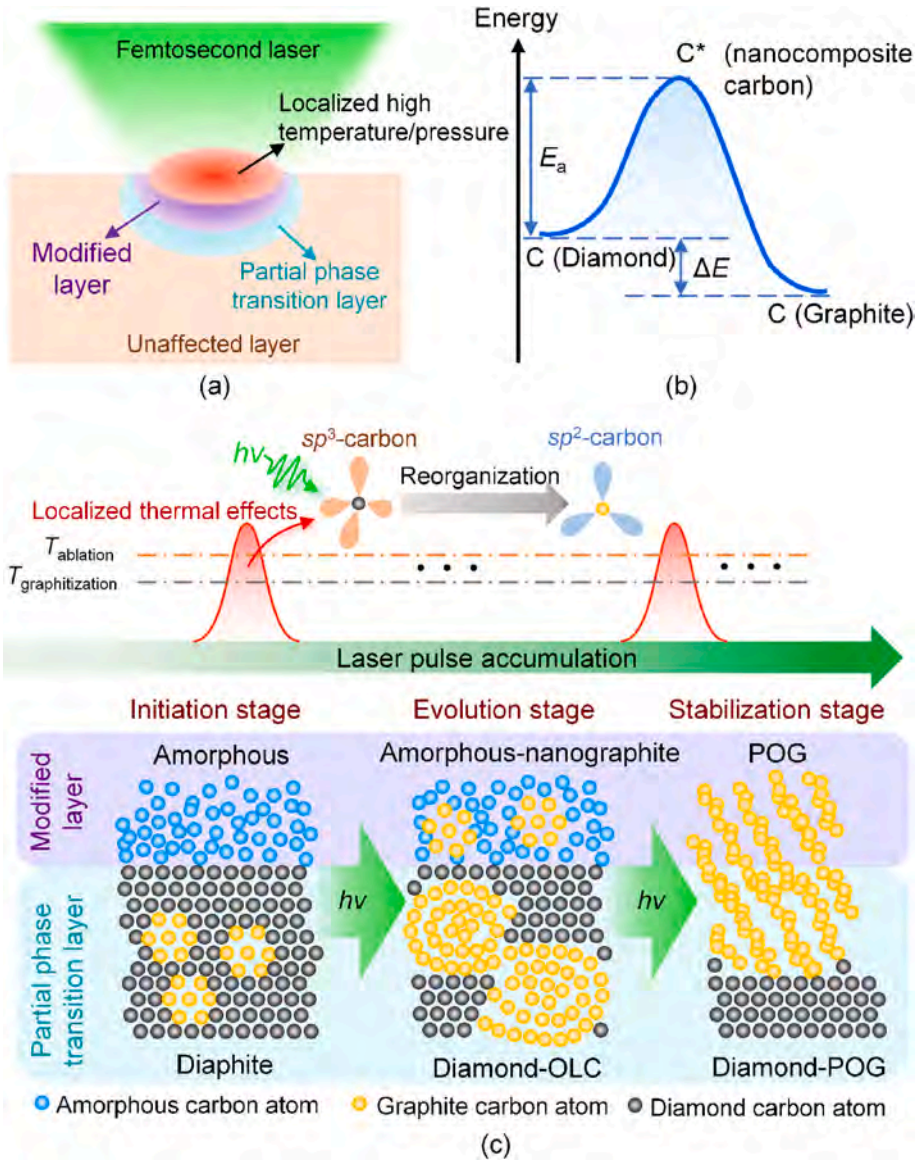

Fig. 11. Schematic diagram of femtosecond laser-induced phase transition mechanisms in diamond. (a) Localized high-temperature and high-pressure environments induced by femtosecond laser processing and the resulting subsurface structures. (b) Reaction coordinate diagram: nanocomposite carbon structures as an intermediate transition pathway reduce the energy barrier for diamond graphitization. (c) Sequential evolution of nanocomposite carbon structures in the modified and partial phase transition layers, illustrating the role of continuous laser pulse energy input and thermal effects in driving the disorder and reorganization of sp^3-carbon to sp^2-carbon.

penetration into the material. The ablation behavior at this stage resembles the graphite piston mode [45], where the surface graphite layer fully absorbs the laser energy and heats up. Subsequent pulses drive this graphite layer downward, acting like a "piston," continuously sublimating the surface material and generating new phase transition interfaces.

The nanocomposite carbon structures formed during irradiation possess lower energy barriers to phase transitions, providing a new pathway for the laser-induced graphitization reaction (Fig. 11b). The sequential evolution mechanism of nanocomposite carbon structures is driven by continuous adaptive restructuring under dynamic feedback from repeated laser pulses and localized thermal effects (as shown in Fig. 11c). These localized thermal effects result from lattice heating due to the diamond's absorption of intense pulses and enhanced absorption from both ablation morphologies and the formed sp^2 graphite layers. Interestingly, the sequential evolution pathway of carbon structures is similar to the structural adjustments observed in diamond during traditional annealing, where the material undergoes reorganization to reduce the system's free energy. While annealing is typically a slow process, gradually achieving phase transitions through the cumulative effects of temperature and time, femtosecond laser significantly shortens this timescale and demonstrates the capability to construct cross-scale micro-nanostructures. These insights not only guide the prediction and control of defects in femtosecond laser processing for various applications but also hold great potential to inspire efficient, precise, and controllable designs of functional carbon materials.

5. Conclusions

Femtosecond laser processing typically requires varying pulse numbers to meet different manufacturing needs. Through multi-pulse experiments and atomic-scale insights into the processed diamond, we have revealed, for the first time, the phase transition mechanism characterized by the sequential evolution of nanocomposite carbon structures. The Two-Temperature Model (TTM) and Finite-Difference Time-Domain (FDTD) simulations further explain the physical origins of these

phase transitions. The main conclusions are summarized as follows:

- Femtosecond laser pulse accumulation leads to continuous structural evolution on the surface and subsurface. Laser-affected layers develop mixed sp^3 and sp^2 bonded nanocomposite carbon structures, characterized by graphite (002) planes merging with diamond (220) planes.
- The formation of diaphite, diamond-OLC (onion-like carbon) phases, along with the transition from amorphous carbon to planar-oriented graphite (POG), observed during sequential evolution, is reported for the first time under femtosecond laser surface processing diamond.
- Ultrafast dynamic cycles drive phase transitions from thermodynamically unstable to stable structures. The distribution of phase transitions is influenced by the near-field enhancement effects resulting from surface nanostructures.
- Graphite nucleation occurs within the diamond matrix rather than at surface defects, facilitated by energy deposition within the bulk and a high-pressure environment. Enhanced absorption by earlier ablation features and rapid lattice heating induced sequential restructuring of nanocarbon structures, leading to a layer of POG at the stable ablation stage.
- The self-evolving pathway of carbon structures shows similarities to the structural adjustments seen in traditional annealing, but the ultrashort timescale of femtosecond laser-induced phase transitions, coupled with the creation of cross-scale surface micro-nanostructures, offers significant potential for designing new functional carbon materials.
- These findings provide a theoretical foundation for optimizing laser parameters to precisely control surface and subsurface structures of diamond, enabling the customization of processes from surface nanopatterning to functionalization and deep material removal.

CRediT authorship contribution statement

Huili Han: Writing – review & editing, Writing – original draft, Software, Methodology, Investigation, Data curation, Conceptualization. **Hao Liu:** Visualization, Investigation. **Jiaxu Huang:** Writing – review & editing, Visualization. **Pei Qiu:** Writing – review & editing, Software. **Jun Li:** Visualization. **Bi Zhang:** Writing – review & editing, Supervision, Project administration, Funding acquisition, Conceptualization. **Shaolin Xu:** Writing – review & editing, Supervision, Project administration, Methodology, Funding acquisition, Conceptualization.

Declaration of competing interest

The authors declare that they have no known competing financial interests or personal relationships that could have appeared to influence the work reported in this paper.

Acknowledgment

The authors acknowledge the assistance of SUSTech Core Research Facilities. This work was financially supported by the National Natural Science Foundation of China (grant no. 52375438), Shenzhen Science and Technology Innovation Commission (grant nos. GJHZ20210705141807023, JCYJ20210324115413036, and JSGG20220831110605009), Guangdong Basic and Applied Basic Research Foundation (2021B1515120009), Shenzhen Science and Technology Program (KJZD20230923115220042), and High level of special funds (G03034K003) from Southern University of Science and Technology.

Appendix 1. Evolution of surface morphology with different pulse energy

The ablated diameter D using a single-pulse condition was measured under varying single-pulse energies E_p, and ω_0 was determined from the linear fit of D^2 versus $\ln(E_P)$, based on the equation $D^2 = 2\omega_0{}^2[\ln(E_P) - \ln(E_{th})]$ [46]. As shown in Fig. A1, ω_0 was extracted from the slope of the fit.

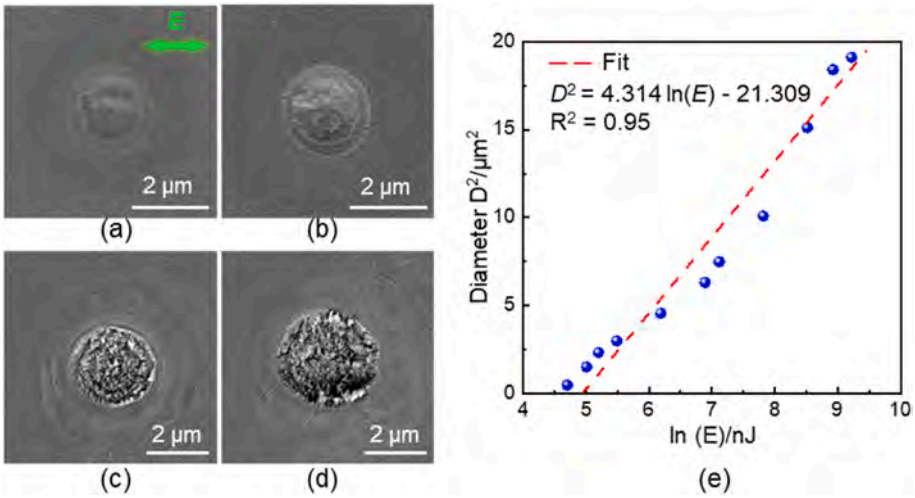

Fig. A1. Evolution of surface morphology under single-pulse irradiation with different pulse energy. (a-d) Single pulse energy is 0.487, 1.23, 7.53, and 12.71 μJ, respectively. Diamond surface fragmentation occurs under high pulse energy irradiation. (e) Functional relationship between the square of the ablation crater diameter and the natural logarithm of the single-pulse energy.

Appendix 2. Preparation of TEM samples by FIB technique

To ensure the consistency and reliability of the experimental results, each set of parameter variations in the laser processing experiments was repeated at least 15 times on three diamond samples. Initial analyses using CCD and optical microscopy were conducted to identify and exclude results potentially affected by laser processing instability. Subsequently, SEM and Raman spectroscopy were performed before FIB and TEM to ensure consistent microstructural evolution and phase transition results across all experimental groups. Multiple TEM lamellae were extracted from samples

processed under identical laser conditions using FIB. Gallium ion beam currents ranging from 9.3 nA to 23 pA, at operating voltage varying from 30 kV to 2 kV, were utilized throughout the initial Pt deposition to sample thinning and final amorphization cleaning.

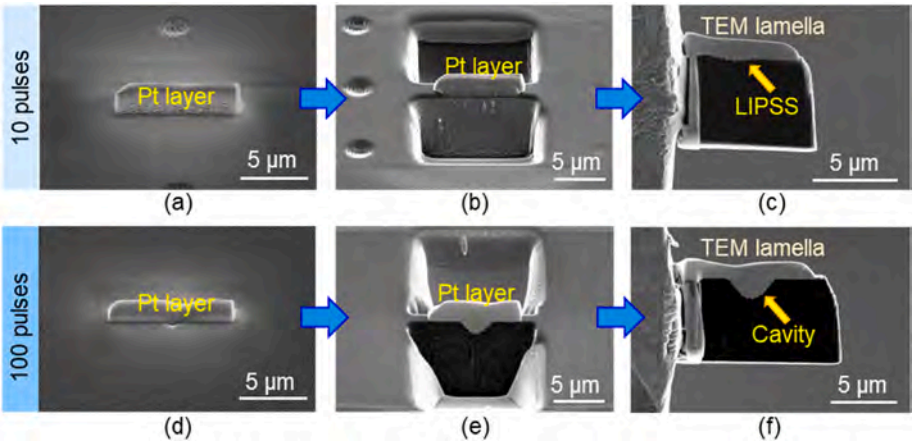

Fig. A2. Preparation of TEM samples by FIB technique. (a, d) Deposition of protective Pt layer on the irradiated structures. (b, e) Location of the cross-section milled by FIB, (c, f) FIB-thinned TEM lamellas.

Appendix 3. Details of ultrafast dynamic process simulation

Considering photoionization and energy loss, the heat source term Q can be expressed as [47]:

$$Q = \left[(h\upsilon - E_g)\frac{\alpha I}{h\upsilon} + (2h\upsilon - E_g)\frac{\beta I}{2h\upsilon} - \eta E_g n_e \right] \frac{n_0 - n_e}{n_0} + \xi I + E_g \frac{n_e}{\tau_m} - \frac{3}{2}\kappa_B T_e \frac{\partial n_e}{\partial t} \quad \text{(EqS1)}$$

where E_g is the bandgap energy, ξ is the free electron absorption coefficient, τ_m is the minimum Auger recombination time, κ_B is Boltzmann constant 1.38×10^{-23} J/K, n_0 is the atomic density of diamond. The incident laser intensity, which is Gaussian distributed in both temporally and spatially, can be calculated as follows [7]:

$$I = \frac{2F_0(1\text{-}R)}{\tau}\sqrt{\frac{\ln 2}{\pi}}\exp\left(-2\frac{r^2}{{\omega_0}^2}\right)\exp\left(-4\ln 2\left(\frac{t\text{-}t_0}{\tau}\right)^2\right) \quad \text{(Eq.S2)}$$

where R is the reflectivity, F_0 is the laser fluence, τ is the pulse duration, r is the radial distance to the center of laser spot, ω_0 is the waist radius, t_0 is the pulse peak time. When diamond is excited to generate a large number of free carriers, the surface optical properties undergo significant changes, affecting the light absorption. Therefore, here we modify the surface reflectance by introducing the Drude model [48], which describes the relationship between optical properties and free electron concentration, to improve the TTM model:

$$\varepsilon^* = -\frac{e^2 n_e \omega \tau_D}{\varepsilon_0 m_0 m_e \omega^2(\omega\tau_D + i)} \quad \text{(Eq.S3)}$$

where ε^* is the dielectric permittivity; ε_0 is the vacuum permittivity, 8.854×10^{-12} F/m; e is the electron charge, 1.6×10^{-19} C; τ_D is the damping time constant; ω is the cyclic frequencies; m_0 is the optical effective mass of the carriers ($m_0 = 0.33$ for diamond); and m_e is the electron mass, 9.109×10^{-31} kg. The reflectivity of the material surface under normal incidence can be calculated using the Fresnel equation [49]:

$$R = \left|\frac{\sqrt{\varepsilon^*} - 1}{\sqrt{\varepsilon^*} + 1}\right| \quad \text{(Eq.S4)}$$

where n and k are the refractive index and extinction coefficient of diamond at 520 nm, defined by $5.89 + 0.00i$. By substituting the reflectivity calculation formula into Eq. S(2), the modified TTM model is obtained.

Based on Eq. (3) and Eqs. S2–S4, the calculated electron density and reflectivity are shown in Fig. A3. The electron density (n_e) peaks at approximately 1.39×10^{21} cm^{-3} within 0.3 ps and then decreases as recombination and diffusion processes dominate. The dynamic change of free carriers directly affects the transient optical properties of diamond under laser irradiation. As shown in Fig. A3b, the initial drop in reflectivity can be explained by the increased absorption due to free carriers. The subsequent energy dissipation decreases the free carrier density, which increases the reflectivity and stabilizes at a new equilibrium.

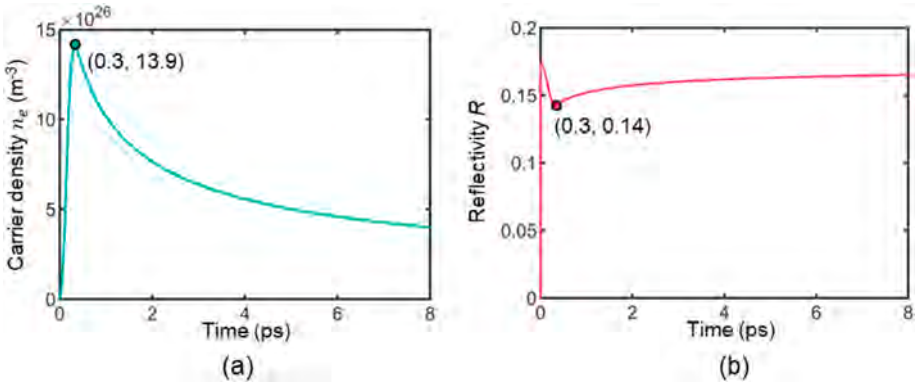

Fig. A3. Physical response of diamond under femtosecond laser irradiation. (a) Temporal evolution of electron density n_e. (b) Temporal evolution of reflectivity R.

Table A1
Initial boundary parameters of the simulation system.

Parameter	Value	Unit
T_e	300	K
T_l	300	K
n_e	1×10^{24}	m^{-3}
dt	1×10^{-16}	s
dx	1×10^{-6}	m

Remark: dt (simulation time step), dx (simulation spatial step).

Table A2
Parameters used in the simulation model [7,47,50,51].

Symbol	Nomenclature	Values	Unit
C_e	Electron heat capacity	$3\kappa_B n_e$	J/(m^3·K)
C_l	Lattice heat capacity	$1.978 \times 10^6 + 354T_l - 3.68 \times 10^6 T_l^{-2}$	W/(m·K)
k_e	Electron thermal conductivity	$-0.556 + 7.13 \times 10^{-3} T_e$	W/(m·K)
k_l	Lattice thermal conductivity	$1.585 \times 10^5 T_l^{-1.23}$	J/(m^3·K)
g	Coupling coefficient	C_e/τ_γ	W/(m^3·K)
τ_γ	Electron-photon coupling time	6.5×10^{-13}	s
D_0	Ambipolar diffusivity	$1.8 \times 10^{-3} \times 300/T_l$	m^2/s
γ	Auger recombination coefficient	3.8×10^{-43}	m^6/s
η	Impact ionization coefficient	$3.6 \times 10^{10} \times e^{\frac{1.5E_0}{k_B T_l}}$	s^{-1}
α	One-photo absorption coefficient	1.021×10^5	m^{-1}
β	Two-photo absorption coefficient	1×10^{-10}	m/W
ξ	Free electron absorption coefficient	$5 \times 10^{-22} T/300$	m^2
τ_m	Minimum Auger recombination time	0.5	ps
E_g	Bandgap energy	$1.86 \times 10^{-19} - 1.123 \times 10^{-22} T_l^2/(T_l + 1108) - 2.4 \times 10^{-29} n_e^{-1/3}$	eV
τ_D	Damping time constant	1.1	fs
$h\nu$	Photon energy	2.38	eV
τ	Pulse duration	300	fs
F_0	Laser fluence	2.06	J/cm^2

Appendix 4. Diamond surface structures evolution with multi-pulse femtosecond laser irradiation

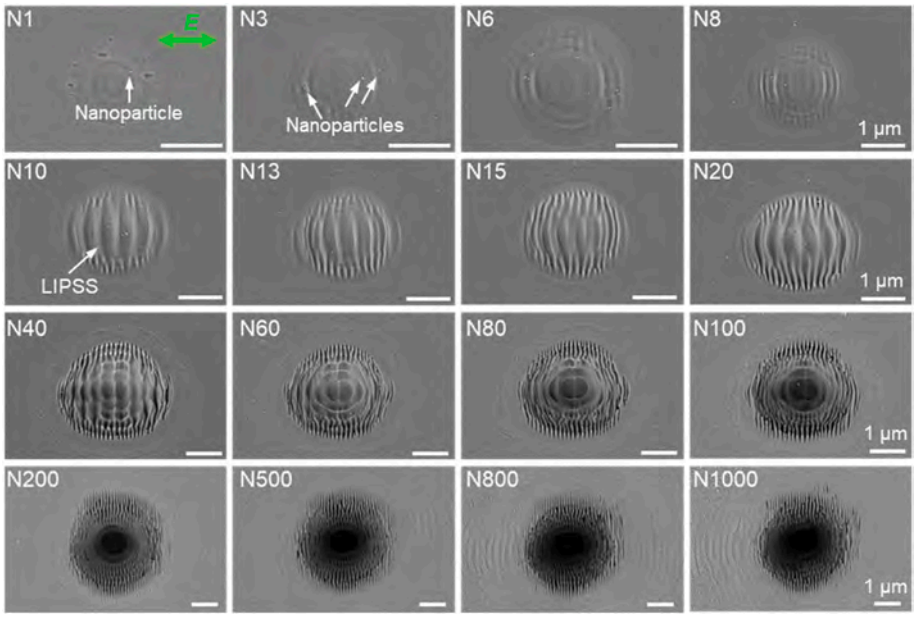

Fig. A4. SEM images of diamond surface structures evolution with multi-pulse femtosecond laser irradiation. The green arrow indicates the polarization direction. The number on each image represents the pulse number.

Appendix 5. Surface reflection state change under microscope illumination

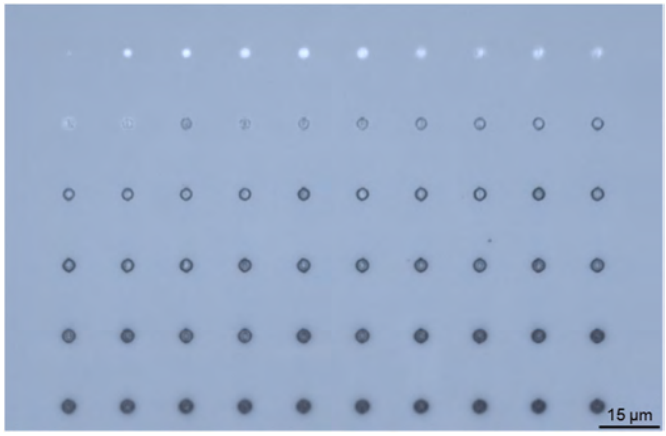

Fig. A5. Surface reflection state changes under microscope illumination when the pulse number accumulates from 1 to 60.

Appendix 6. Surface morphology evolution with different pulse intervals

The surface morphology in point processing with pulse intervals ranging from 100 to 0.1 ms exhibits a consistent change trend as the pulse number accumulates. The single-pulse energy was fixed at 242.8 nJ, corresponding to a peak fluence of 7.16 J cm^{-2}.

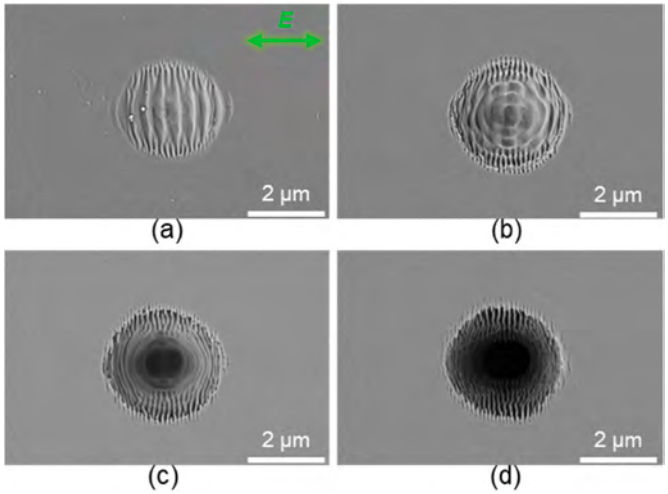

Fig. A6. SEM images of surfaces irradiated with (a) 20, (b) 50, (c) 100, and (d) 500 pulses, 100 ms pulse interval.

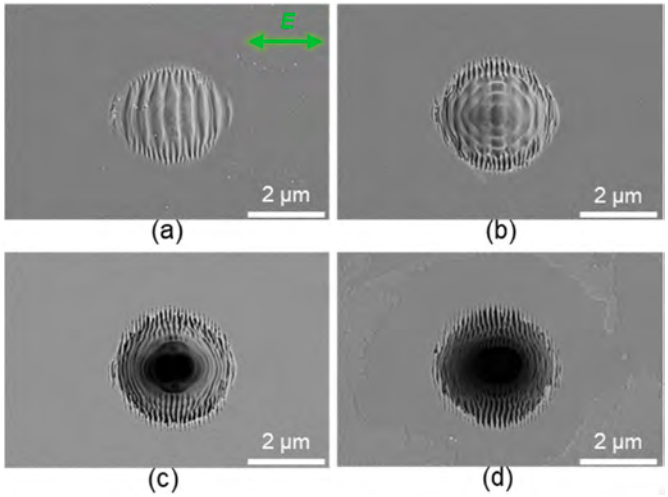

Fig. A7. SEM images of surfaces irradiated with (a) 20, (b) 50, (c) 100, and (d) 500 pulses, 10 ms pulse interval.

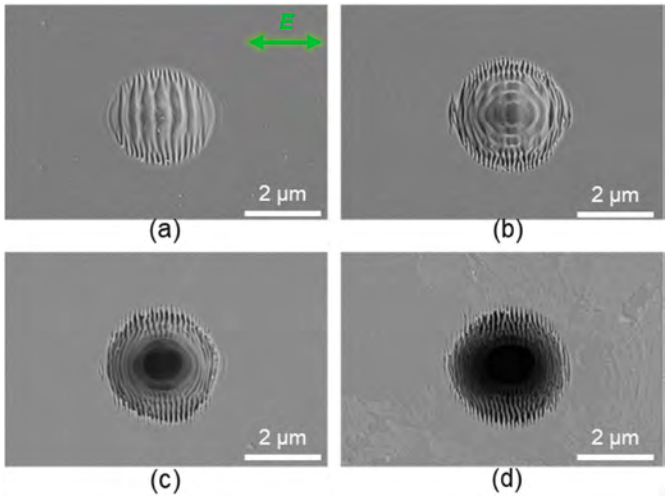

Fig. A8. SEM images of surfaces irradiated with (a) 20, (b) 50, (c) 100, and (d) 500 pulses, 1 ms pulse interval.

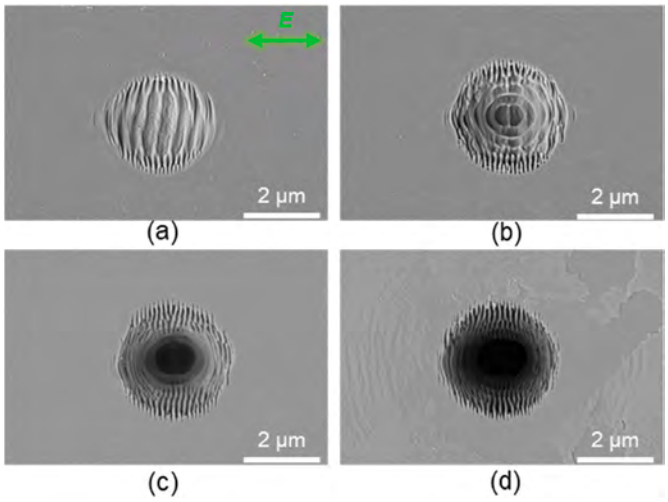

Fig. A9. SEM images of surfaces irradiated with (a) 20, (b) 50, (c) 100, and (d) 500 pulses, 0.1 ms pulse interval.

Appendix 7. Raman spectra with different pulse intervals

The Raman spectra with different pulse intervals consistently exhibit an sp^3 diamond peak and a broad band resulting from merging the D and G peaks associated with sp^2 carbon. The only variation is in the relative content of the graphite-like phase. This consistency demonstrates the broad applicability of the phase transition conclusions discussed in this work across a wide range of femtosecond laser processing conditions.

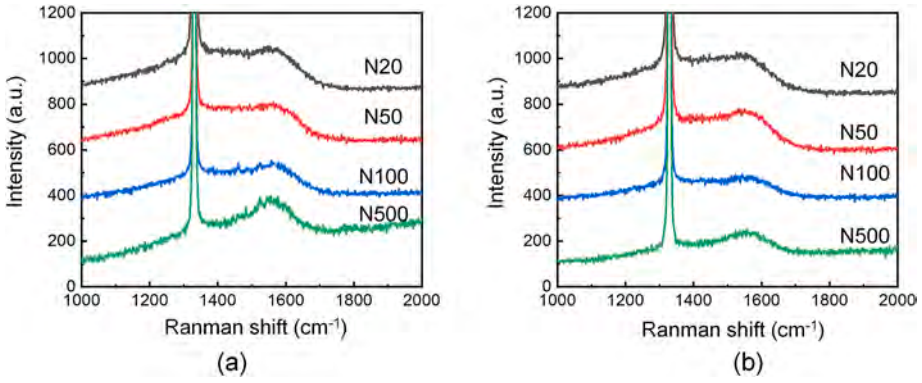

Fig. A10. Raman spectra with different pulse intervals. (a) 100 ms, (b) 0.1 ms.

Data availability

Data will be made available on request.

References

[1] Y. Wan, J.-H. Fu, C.-P. Chuu, V. Tung, Y. Shi, L.-J. Li, Wafer-scale single-orientation 2D layers by atomic edge-guided epitaxial growth, Chem. Soc. Rev. 51 (2022) 803–811, https://doi.org/10.1039/D1CS00264C.

[2] Y.-C. Chen, P.S. Salter, S. Knauer, L. Weng, A.C. Frangeskou, C.J. Stephen, S. N. Ishmael, P.R. Dolan, S. Johnson, B.L. Green, G.W. Morley, M.E. Newton, J. G. Rarity, M.J. Booth, J.M. Smith, Laser writing of coherent colour centres in diamond, Nat. Photonics 11 (2017) 77–80, https://doi.org/10.1038/nphoton.2016.234.

[3] C. Dang, J.-P. Chou, B. Dai, C.-T. Chou, Y. Yang, R. Fan, W. Lin, F. Meng, A. Hu, J. Zhu, J. Han, A.M. Minor, J. Li, Y. Lu, Achieving large uniform tensile elasticity in microfabricated diamond, Science 371 (2021) 76–78, https://doi.org/10.1126/science.abc4174.

[4] V.I. Konov, Laser in micro and nanoprocessing of diamond materials, Laser Photon. Rev. 6 (2012) 739–766, https://doi.org/10.1002/lpor.201100030.

[5] B. Ali, I.V. Litvinyuk, M. Rybachuk, Femtosecond laser micromachining of diamond: current research status, applications and challenges, Carbon 179 (2021) 209–226, https://doi.org/10.1016/j.carbon.2021.04.025.

[6] S.K. Sundaram, E. Mazur, Inducing and probing non-thermal transitions in semiconductors using femtosecond laser pulses, Nat. Mater. 1 (2002) 217–224, https://doi.org/10.1038/nmat767.

[7] Y. Liu, Y. Ding, J. Xie, L. Xu, I. Wha Jeong, L. Yang, One-step femtosecond laser irradiation of single-crystal silicon: evolution of micro-nano structures and damage investigation, Mater. Des. 225 (2023) 111443, https://doi.org/10.1016/j.matdes.2022.111443.

[8] Z.U. Rehman, K.A. Janulewicz, Structural transformations in femtosecond laser-processed n-type 4H-SiC, Appl. Surf. Sci. 385 (2016) 1–8, https://doi.org/10.1016/j.apsusc.2016.05.041.

[9] M.J. Smith, Y.-T. Lin, M.-J. Sher, M.T. Winkler, E. Mazur, S. Gradečak, Pressure-induced phase transformations during femtosecond-laser doping of silicon, J. Appl. Phys. 110 (2011) 053524, https://doi.org/10.1063/1.3633528.

[10] J. Zhao, C. Zhang, F. Liu, G.J. Cheng, Understanding femtosecond laser internal scribing of diamond by atomic simulation: phase transition, structure and property, Carbon 175 (2021) 352–363, https://doi.org/10.1016/j.carbon.2021.01.111.

[11] B. Sotillo, V. Bharadwaj, J.P. Hadden, M. Sakakura, A. Chiappini, T.T. Fernandez, S. Longhi, O. Jedrkiewicz, Y. Shimotsuma, L. Criante, R. Osellame, G. Galzerano, M. Ferrari, K. Miura, R. Ramponi, P.E. Barclay, S.M. Eaton, Diamond photonics platform enabled by femtosecond laser writing, Sci. Rep. 6 (2016) 35566, https://doi.org/10.1038/srep35566.

[12] B. Ali, H. Xu, R.T. Sang, I.V. Litvinyuk, M. Rybachuk, Optimised diamond to graphite conversion via a metastable sp1-bonded carbon chain formation under an ultra-short femtosecond (30 fs) laser irradiation, Carbon 204 (2023) 575–586, https://doi.org/10.1016/j.carbon.2023.01.012.

[13] P. Németh, K. McColl, L.A.J. Garvie, C.G. Salzmann, M. Murri, P.F. McMillan, Complex nanostructures in diamond, Nat. Mater. 19 (2020) 1126–1131, https://doi.org/10.1038/s41563-020-0759-8.
[14] P. Németh, K. McColl, R.L. Smith, M. Murri, L.A.J. Garvie, M. Alvaro, B. Pécz, A. P. Jones, F. Corà, C.G. Salzmann, P.F. McMillan, Diamond-graphene composite nanostructures, Nano Lett. 20 (2020) 3611–3619, https://doi.org/10.1021/acs.nanolett.0c00556.
[15] E.M. Hsu, N.A. Mailman, G.A. Botton, H.K. Haugen, Microscopic investigation of single-crystal diamond following ultrafast laser irradiation, Appl. Phys. A 103 (2011) 185–192, https://doi.org/10.1007/s00339-010-5986-4.
[16] Z.U. Rehman, K.A. Janulewicz, Structural transformation of monocrystalline diamond driven by ultrashort laser pulses, Diam. Relat. Mater. 70 (2016) 194–200, https://doi.org/10.1016/j.diamond.2016.11.004.
[17] P.S. Salter, M.P. Villar, F. Lloret, D.F. Reyes, M. Krueger, C.S. Henderson, D. Araujo, R.B. Jackman, Laser engineering nanocarbon phases within diamond for science and electronics, ACS Nano (2024) 3c07116, https://doi.org/10.1021/acsnano.3c07116, acsnano.
[18] L. Huang, K. Xu, D. Yuan, J. Hu, X. Wang, S. Xu, Sub-wavelength patterned pulse laser lithography for efficient fabrication of large-area metasurfaces, Nat. Commun. 13 (2022) 5823, https://doi.org/10.1038/s41467-022-33644-8.
[19] Y. Guo, P. Qiu, S. Xu, G.J. Cheng, Laser-induced microjet-assisted ablation for high-quality microfabrication, Int. J. Extrem. Manuf. 4 (2022) 035101, https://doi.org/10.1088/2631-7990/ac6632.
[20] F.C.B. Maia, R.E. Samad, J. Bettini, R.O. Freitas, N.D. Vieira Junior, N.M. Souza-Neto, Synthesis of diamond-like phase from graphite by ultrafast laser driven dynamical compression, Sci. Rep. 5 (2015) 11812, https://doi.org/10.1038/srep11812.
[21] D. Ramanathan, P.A. Molian, Micro- and sub-micromachining of type IIa single crystal diamond using a Ti:sapphire femtosecond laser, J. Manuf. Sci. Eng. 124 (2002) 389–396, https://doi.org/10.1115/1.1459083.
[22] P. Boerner, M. Hajri, N. Ackerl, K. Wegener, Experimental and theoretical investigation of ultrashort pulsed laser ablation of diamond, J. Laser Appl. 31 (2019) 22202, https://doi.org/10.2351/1.5096088.
[23] J. Yin, G. Chen, Z. Zhu, M. Jin, B. Hu, Ablation mechanism investigation and ablation threshold prediction of single crystal diamond irradiated by femtosecond laser, Diam. Relat. Mater. 111 (2021) 108173, https://doi.org/10.1016/j.diamond.2020.108173.
[24] H. Vaghasiya, S. Krause, P.-T. Miclea, Thermal and non-thermal ablation mechanisms in crystalline silicon by femtosecond laser pulses: classical approach of the carrier density two temperature model, J. Phys. D Appl. Phys. 55 (2022) 175109, https://doi.org/10.1088/1361-6463/ac4dca.
[25] J. Huang, K. Xu, S. Xu, X. Li, Q. Wei, Self-aligned laser-induced periodic surface structures for large-area controllable nanopatterning, Laser Photon. Rev. 16 (2022) 2200093, https://doi.org/10.1002/lpor.202200093.
[26] J. Xie, J. Yan, D. Zhu, G. He, Atomic-level insight into the Formation of subsurface dislocation layer and its effect on mechanical properties during ultrafast laser micro/nano fabrication, Adv. Funct. Mater. 32 (2022) 2108802, https://doi.org/10.1002/adfm.202108802.
[27] D.S. Knight, W.B. White, Characterization of diamond films by Raman spectroscopy, J. Mater. Res. 4 (1989) 385–393, https://doi.org/10.1557/JMR.1989.0385.
[28] X.J. Hu, Y.G. Shen, X.P. Hao, B.Y. Wang, The structural properties of B–O codoped diamond films, Diam. Relat. Mater. 18 (2009) 210–212, https://doi.org/10.1016/j.diamond.2008.07.009.
[29] D.P. Hickey, K.S. Jones, R.G. Elliman, Amorphization and graphitization of single-crystal diamond — a transmission electron microscopy study, Diam. Relat. Mater. 18 (2009) 1353–1359, https://doi.org/10.1016/j.diamond.2009.08.012.
[30] S. Rubanov, A. Suvorova, V.P. Popov, A.A. Kalinin, Yu.N. Pal'yanov, Fabrication of graphitic layers in diamond using FIB implantation and high pressure high temperature annealing, Diam. Relat. Mater. 63 (2016) 143–147, https://doi.org/10.1016/j.diamond.2015.11.017.
[31] J. Qian, C. Pantea, J. Huang, T.W. Zerda, Y. Zhao, Graphitization of diamond powders of different sizes at high pressure–high temperature, Carbon 42 (2004) 2691–2697, https://doi.org/10.1016/j.carbon.2004.06.017.
[32] V.D. Blank, B.A. Kulnitskiy, A.A. Nuzhdin, Lonsdaleite formation in process of reverse phase transition diamond–graphite, Diam. Relat. Mater. 20 (2011) 1315–1318, https://doi.org/10.1016/j.diamond.2011.08.009.
[33] O. Mykhailiv, H. Zubyk, M.E. Plonska-Brzezinska, Carbon nano-onions: unique carbon nanostructures with fascinating properties and their potential applications, Inorg. Chim. Acta. 468 (2017) 49–66, https://doi.org/10.1016/j.ica.2017.07.021.
[34] S. Zhang, Q. Zhang, Z. Liu, D. Legut, T.C. Germann, S. Veprek, H. Zhang, R. Zhang, Ultrastrong π-bonded interface as ductile plastic flow channel in nanostructured diamond, ACS Appl. Mater. Interfaces 12 (2020) 4135–4142, https://doi.org/10.1021/acsami.9b19725.
[35] K.M. Tripathi, T.S. Tran, Y.-J. Kim, T. Kim, Green fluorescent onion-like carbon nanoparticles from flaxseed oil for visible light induced photocatalytic applications and label-free detection of Al(III) ions, ACS Sustainable Chem. Eng. 5 (2017) 3982–3992, https://doi.org/10.1021/ACSSUSCHEMENG.6B03182.
[36] J.K. McDonough, A.I. Frolov, V. Presser, J. Niu, C.H. Miller, T. Ubieto, M. V. Fedorov, Y. Gogotsi, Influence of the structure of carbon onions on their electrochemical performance in supercapacitor electrodes, Carbon 50 (2012) 3298–3309, https://doi.org/10.1016/j.carbon.2011.12.022.
[37] E.D. Obraztsova, M. Fujii, S. Hayashi, V.L. Kuznetsov, Yu.V. Butenko, A. L. Chuvilin, Raman identification of onion-like carbon, Carbon 36 (1998) 821–826, https://doi.org/10.1016/S0008-6223(98)00014-1.
[38] B. Yan, N. Chen, Y. Zhu, Y. Yang, G. Zhao, W. Zhao, X. Hao, L. Li, L. Wang, E. Abele, N. He, Instantaneous formation of covalently bonded diamond–graphite–graphene with synergistic properties, Int. J. Mach. Tool Manufact. 193 (2023) 104087, https://doi.org/10.1016/j.ijmachtools.2023.104087.
[39] L. Liu, F. Lu, J. Tian, S. Xia, Y. Diao, Electronic and optical properties of amorphous carbon with different sp3/sp2 hybridization ratio, Appl. Phys. A 125 (2019) 366, https://doi.org/10.1007/s00339-019-2660-3.
[40] Y. Rho, H. Kang, C.P. Grigoropoulos, K.-T. Kang, Site-selective synthesis of onion like carbon from nanodiamond thin film via laser-assisted photothermal process, Appl. Phys. A 126 (2020) 703, https://doi.org/10.1007/s00339-020-03875-x.
[41] H. Xie, B. Zhao, J. Cheng, S.K. Chamoli, T. Zou, W. Xin, J. Yang, Super-regular femtosecond laser nanolithography based on dual-interface plasmons coupling, Nanophotonics 10 (2021) 3831–3842, https://doi.org/10.1515/nanoph-2021-0329.
[42] V.V. Kononenko, V.M. Gololobov, T.V. Kononenko, V.I. Konov, Photoinduced graphitization of diamond, Laser Phys. Lett. 12 (2015) 016101, https://doi.org/10.1088/1612-2011/12/1/016101.
[43] P. Németh, L.A.J. Garvie, Extraterrestrial, shock-formed, cage-like nanostructured carbonaceous materials, Am. Mineral. 105 (2020) 276–281, https://doi.org/10.2138/am-2020-7305.
[44] B. Guo, J. Sun, Y. Lu, L. Jiang, Ultrafast dynamics observation during femtosecond laser-material interaction, Int. J. Extrem. Manuf. 1 (2019) 032004, https://doi.org/10.1088/2631-7990/ab3a24.
[45] V.V. Kononenko, Modification of diamond surface by femtosecond laser pulses, Photonics 10 (2023) 1077, https://doi.org/10.3390/photonics10101077.
[46] J.M. Liu, Simple technique for measurements of pulsed Gaussian-beam spot sizes, Opt. Lett. 7 (1982) 196, https://doi.org/10.1364/OL.7.000196.
[47] N.M. Bulgakova, R. Stoian, A. Rosenfeld, I.V. Hertel, W. Marine, E.E.B. Campbell, A general continuum approach to describe fast electronic transport in pulsed laser irradiated materials: the problem of Coulomb explosion, Appl. Phys. A 81 (2005) 345–356, https://doi.org/10.1007/s00339-005-3242-0.
[48] L. Wang, Q.-D. Chen, X.-W. Cao, R. Buividas, X. Wang, S. Juodkazis, H.-B. Sun, Plasmonic nano-printing: large-area nanoscale energy deposition for efficient surface texturing, Light Sci. Appl. 6 (2017) e17112, https://doi.org/10.1038/lsa.2017.112.
[49] E. Petrakakis, G.D. Tsibidis, E. Stratakis, Modelling of the ultrafast dynamics and surface plasmon properties of silicon upon irradiation with mid-IR femtosecond laser pulses, Phys. Rev. B 99 (2019) 195201, https://doi.org/10.1103/PhysRevB.99.195201.
[50] T. Roth, R. Laenen, Absorption of free carriers in diamond determined from the visible to the mid-infrared by femtosecond two-photon absorption spectroscopy, Opt Commun. 189 (2001) 289–296, https://doi.org/10.1016/S0030-4018(01)01037-9.
[51] X. Zhang, F. Wang, L. Jiang, Y. Yao, Manipulation of the dielectric properties of diamond by an ultrashort laser pulse, Phys. Rev. B 95 (2017) 184301, https://doi.org/10.1103/PhysRevB.95.184301.